WILEY | Hindawi

Research Article

Feasibility of Tunnel TEM Advanced Prediction: A 3D Forward Modeling Study

Jiannan Fu [ID],[1] Xiaodong Yang [ID],[2] Guanqun Zhou [ID],[3] Xueliang Jin [ID],[4] Fuqin Zhai [ID],[5] Fanbin Meng [ID],[6] and Yafei Wang [ID][3]

[1]*School of Geosciences and Surveying Engineering, China University of Mining and Technology (Beijing), Beijing 100083, China*
[2]*School of Earth and Space Sciences, University of Science and Technology of China, Hefei 230026, China*
[3]*School of Resources and Environmental Engineering, Hefei University of Technology, Hefei 230009, China*
[4]*School of Resources and Geosciences, China University of Mining and Technology, Xuzhou 221116, China*
[5]*Anhui Huizhou Geology Security Institute Co., Ltd., Hefei 230088, China*
[6]*Research Institute of Coal Geophysical Exploration, China National Administration of Coal Geology, Zhuozhou 072750, China*

Correspondence should be addressed to Guanqun Zhou; guanqun@mail.ustc.edu.cn

The transient electromagnetic (TEM) method has long been applied in tunnel advanced prediction. However, it remains questionable to what extent a geologic anomaly body will influence the induced electromagnetic response in front of the heading face. The dilemma is partly because observed TEM data are frequently interpreted by empirical formulas or proportional relationships, and a quantitative measurement has not been established. In this paper, we strive to understand the TEM characteristics from a 3D finite-element time-domain (FETD) modeling aspect. The modeling algorithm is based on unstructured space meshing and unconditional stable time discretization, which ensures its accuracy and stability. The modeling algorithm is verified by a half-space model, in which the misfit of late-time channels that we are concerned with is generally below 1%. The algorithm has also been utilized to carry out the TEM response of tunnel models with different types of TEM devices. Through model studies, we find that both the traditional central-loop device and the recently developed weak-coupling opposing-coil device are feasible in tunnel advanced detection. Nevertheless, the latter type of device better distinguishes low-resistivity anomalies at 30 m ahead of the heading face with a relative difference (between models with and without the anomaly) of more than 1000% at certain time channels, compared with only a 10% difference of the central-loop device. Also, we conclude that the vertical electromagnetic field component should be recorded and interpreted together with the horizontal field to provide more convincing results.

1. Introduction

The tunnel advanced prediction method is aimed at determining blind faults, karsts, and other geologic bodies ahead of the working face [1]. Several types of geophysical prospecting methods, including seismic tomography [2], reverse time migration [3], direct current electric sounding [4], magnetic resonance sounding [5], and the transient electromagnetic (TEM, also called time-domain electromagnetic, TDEM) method [6], have been applied to tunnel advanced prediction. Among them, electromagnetic methods have the unique advantage that they are more sensitive to the

composition of heading rocks rather than the distribution of geologic interfaces [7]. More explicitly, electromagnetic surveys can help find water-bearing faults and karsts with relatively high electric conductivity [8]. Thus, they play a crucial role in preventing water inrush disasters and protecting lives and property during the tunnel excavation process.

As one of the electromagnetic methods, the TEM method was first proposed by Keller in 1969 [9]. Since then, the TEM method has found an increasingly wide utilization, including the long-offset TEM method with dipole source [10], the land big-loop TEM method with square coil source [11], and the airborne TEM method with circular coil source

[12]. The TEM method has shown its advantage at sites where space is highly limited since the transmission of pulse-type electromagnetic signals does not require a high-power device. The above aspects prompt applying the TEM method in tunnel advanced detection, and it has thrived over the past two decades [13–16]. However, most of these interpretation results were carried out through empirical relationships between the buried depth of the geologic body and the arrival time of the electromagnetic wave. And thus, the geophysical society still holds the question of whether the response at a certain time point is caused by a specific anomaly body or, comparatively, to what extent the anomaly body will influence the recorded field.

3D modeling provides explicit theoretical support for geoprospecting methods on a physical basis. In the time domain, electromagnetic modeling is often carried out by the finite-difference time-domain (FDTD) method and the finite-element time-domain (FETD) method. With the FDTD method, the calculation domain is discretized with structured meshes, and a conditionally stable time-stepping technique is required [17]. In comparison, the FETD method allows unstructured meshing that can accurately fit the terrain and irregular geologic bodies [18]. And by introducing unconditionally stable stepping methods, the FETD method allows larger step size in late-time simulation, and thus, much fewer time steps are required [19]. These advantages of the FETD method ensure both its computational accuracy and efficiency and make it suitable for geoelectromagnetic modeling.

In the specific application of tunnel advanced prediction, an appropriate design of the TEM device is also crucial. For instance, it has been reported that TEM data at early time channels are sophisticated with primary-field disturbances, which may further result in a blind zone at shallow depths [20]. Meanwhile, the mutual inductance problem arises with the traditional central-loop device, as multiturn wires are twined tightly with each other [21]. To address these issues, weak-coupling TEM devices have recently been developed [22, 23]. And in this paper, TEM responses of both types of device are calculated to further confirm the feasibility of tunnel advanced prediction using the TEM method. In the following sections, the proposed 3D FETD algorithm is first illustrated, and its accuracy is verified by a half-space analytical solution. The feasibility study is then conducted through various model simulations.

2. Methods

With Faraday's law

$$\nabla \times \mathbf{E} + \mu \frac{\partial \mathbf{H}}{\partial t} = 0 \tag{1}$$

and Ampère's law

$$\nabla \times \mathbf{H} + \epsilon \frac{\partial \mathbf{E}}{\partial t} = \sigma \mathbf{E} + \mathbf{J}, \tag{2}$$

we acquire the vector electromagnetic wave equation as

$$\nabla \times \left(\frac{1}{\mu} \nabla \times \mathbf{E} \right) + \epsilon \frac{\partial^2 \mathbf{E}}{\partial t^2} + \sigma \frac{\partial \mathbf{E}}{\partial t} + \frac{\partial \mathbf{J}}{\partial t} = 0. \tag{3}$$

In these formulas, $\mathbf{J}$ represents the external current source, in our case, the TEM source of the system. μ, ϵ, and σ are the magnetic permeability, the dielectric permittivity, and the electric conductivity of the medium, respectively. A rational approximation in low-frequency geoelectromagnetic simulation is to eliminate the second derivative term in Equation (1) [24], which gives

$$\nabla \times \left(\frac{1}{\mu} \nabla \times \mathbf{E} \right) + \sigma \frac{\partial \mathbf{E}}{\partial t} + \frac{\partial \mathbf{J}}{\partial t} = 0. \tag{4}$$

In the above equation, the boundary condition of a perfect electrical conductor

$$\mathbf{n} \times (\nabla \times \mathbf{E})|_\Gamma = 0 \tag{5}$$

on the domain boundary Γ and the initial condition

$$\mathbf{E}|_{t=0} = 0 \tag{6}$$

give the boundary-initial value problem to solve.

2.1. Discretization in Space and Time. Following the classical finite element method [25], we have the system of equations as

$$\mathbf{A} \frac{d\mathbf{E}}{dt} + \mathbf{CE} = \mathbf{S}. \tag{7}$$

Here, $\mathbf{E}$ represents the global electric field vector under the vector finite element basis [26]. With this set of basis functions, the electric field to be measured can be approximated by

$$\mathbf{E} \approx \sum_{j=1}^{n_{\text{edge}}} \mathbf{N}_j E_j, \tag{8}$$

where n_{edge} is the total edge number of the discretized domain. And global integral matrices $\mathbf{A}$, $\mathbf{C}$, and $\mathbf{S}$ have the form of

$$\mathbf{A} = \sum_\Omega \int_{\Omega^e} \sigma^e \mathbf{N}_i^e \cdot \mathbf{N}_j^e d\Omega, \tag{9}$$

$$\mathbf{C} = \sum_\Omega \int_{\Omega^e} \frac{1}{\mu^e} \left(\nabla \times \mathbf{N}_i^e \right) \cdot \left(\nabla \times \mathbf{N}_j^e \right) d\Omega, \tag{10}$$

$$\mathbf{S} = -\sum_\Omega \int_{\Omega^e} \mathbf{N}_i^e \cdot \frac{\partial \mathbf{J}^e}{\partial t} d\Omega, \tag{11}$$

where the superscript e represents a local element and Ω represents the whole simulation domain.

To discretize the ODE system (Equation (7)) in the time domain, we apply the unconditionally stable Newmark-β method with $\beta = 1/4$ [27] and obtain a time-stepping equation

$$\mathbf{P}\mathbf{E}^n = \mathbf{S}^{n-1} - \mathbf{Q}\mathbf{E}^{n-1} - \mathbf{R}\mathbf{E}^{n-2}, \tag{12}$$

where $\mathbf{E}^n$ represents the field vector at the nth step. The stepping matrices $\mathbf{P}$, $\mathbf{Q}$ and $\mathbf{R}$ have the form of

$$\mathbf{P} = \frac{\mathbf{A}}{2\Delta t} + \frac{\mathbf{C}}{4},$$
$$\mathbf{Q} = \frac{\mathbf{C}}{2}, \tag{13}$$
$$\mathbf{R} = -\frac{\mathbf{A}}{2\Delta t} + \frac{\mathbf{C}}{4},$$

where Δt is the current step size.

In TEM modeling, specifically, Um et al. [28] pointed out that fixed step size cannot cover the wide time magnitudes from early-time transient response to late-time diffusive field, and thus a step-changing scheme should be imposed. Based on this, the initial step is defined as $\Delta t_0 = t_p/20$ in which t_p represents the pulse width of the TEM source, and we double Δt every 25 steps in this research to ensure stability. It is also worth noticing that within these steps at which Δt does not change, the sparse matrices $\mathbf{P}$, $\mathbf{Q}$, and $\mathbf{R}$ also keep unchanged. Therefore, the symbolic factorization [29] of $\mathbf{P}$, which is the most time-consuming part of 3D TEM modeling, is only performed a limited (typically less than 20) times throughout the simulation. Finally, the electric field is calculated by Equation (8), and the induced electromotive force in a certain direction $\mathbf{n}$ is derived by

$$\varepsilon = \mathbf{n} \cdot \frac{\partial \mathbf{B}}{\partial t} \approx -\mathbf{n} \cdot \sum_{j=1}^{n_{\text{edge}}} \left(\nabla \times \mathbf{N}_j \right) E_j. \tag{14}$$

If needed, the total magnetic field at a specific time point t_c can then be deduced by the time integral.

$$\mathbf{B}\big|_{t_c} = \int_{t=0}^{t_c} \frac{\partial \mathbf{B}}{\partial t}\, \mathrm{dt}. \tag{15}$$

2.2. Numerical Implementation. The construction of the source term (Equation (11)) is challenging. Since if the wire passes through an element arbitrarily, a complicated integral has to be carried out. One simplification is to directly subdivide the transmitting wire, by which the element integral only has to be calculated on the edges. With this consideration, Equation (11) could be rewritten as

$$\mathbf{S} = -\sum_{\Omega} \mathbf{N}_I \cdot \hat{\mathbf{n}}_I \frac{d^2 p}{\mathrm{dt}^2}, \tag{16}$$

in which the subscript I denotes the global edges that the source wire lays on. $\hat{\mathbf{n}}$ is the direction of the current, and

$\mathbf{N}_I \cdot \hat{\mathbf{n}}_I$ values 1 when $\mathbf{N}_I$ and $\hat{\mathbf{n}}_I$ are in the same direction and values -1 when they are in the opposite direction [30]. In the above equation, the relationship

$$\mathbf{J} = \hat{\mathbf{n}} J = \hat{\mathbf{n}} \frac{\mathrm{dp}}{\mathrm{dt}} \tag{17}$$

holds, and p represents the electric moment of the source. As a typical pulse type used in TEM signal transmission, the step pulse is simulated in this research. We approximately formulate the unit step pulse with [31].

$$p(t) = 0.5\,\mathrm{erf}\left[\frac{5\left(t - 0.5 t_p\right)}{t_p}\right] + 0.5, \tag{18}$$

where erf represents the error function.

In this paper, 3D unstructured tetrahedral meshing is applied, and the open-source software Gmsh is used to generate the consequent Delaunay triangulation [32, 33]. With this said, the two types of TEM devices of our concern are illustrated in Figure 1. It can be seen from Figure 1(a) that $\hat{\mathbf{n}}$ always has the same direction within a single coil, yet $\mathbf{N}$ points from the node with a lower identifier to the node with a higher identifier according to a common definition [30]. Thus, $\mathbf{N} \cdot \hat{\mathbf{n}}$ equals -1 on the edge that links points 1 and 26, and it equals 1 elsewhere with regard to this example. Hereinafter, the traditional small-loop TEM device with one transmitting coil shown in Figure 1(a) is referred to as the single-TX device, and the device with two opposing coils shown in Figure 1(b) is referred to as the opposing-TX device.

In a typical 3D geoelectromagnetic modeling problem, the total edge number can reach up to several million. And specific to the time-domain variation, an iteration over several hundreds of time steps has to be calculated. Therefore, the efficient solving of the huge sparse system occupies a pivotal place in the simulation. A sparse system is traditionally solved by iterative solvers, and various types of algorithms have been developed [34]. However, the iterative method has several drawbacks when solving a system with an extremely ill-conditioned left-hand side matrix or multiple right-hand side vectors. With a direct solver, comparatively, the sparse matrix is first handled by numerical factorization, and solutions of different right-hand sides are then derived by forward and backward substitution [35]. This separate design of the direct solver services our needs as stated in the above-proposed algorithm. And PARDISO [36], a parallel realization of direct sparse solver, is applied in this research. The performance of the sparse linear algebra library is also crucial to the overall computational time of 3D TEM modeling. In our program, the construction of sparse system matrices, the addition of sparse matrices, and the sparse matrix-vector multiplication are realized by a high-performance sparse BLAS library [37]. The following simulations are carried out with an 8-core Intel I7-11700 CPU.
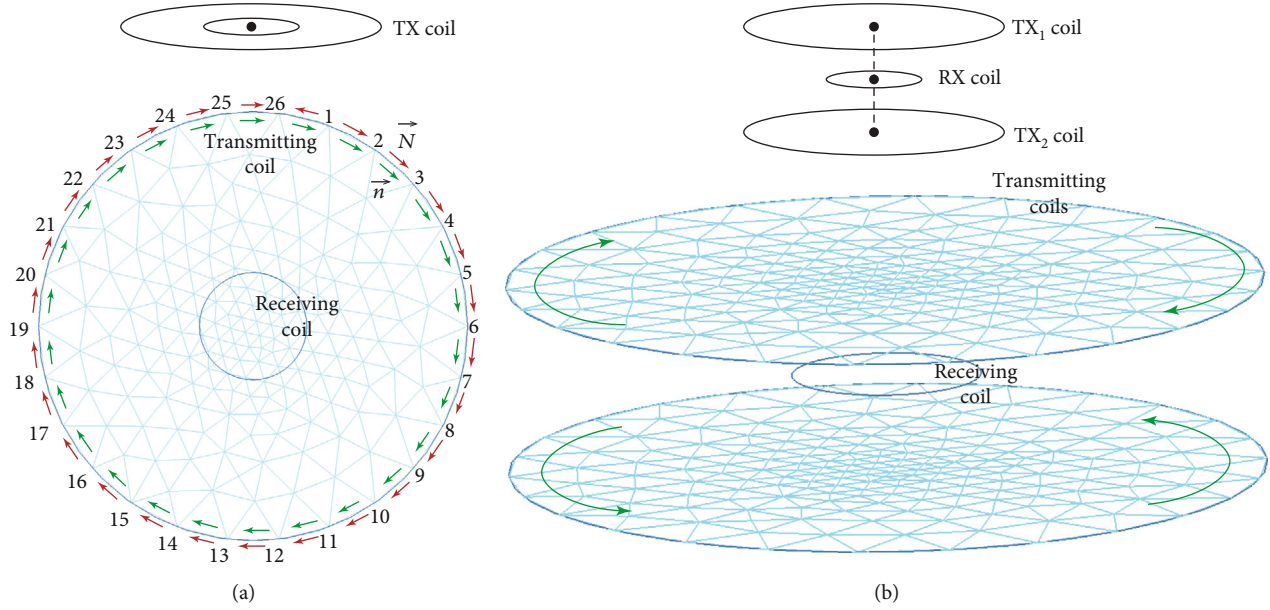
FIGURE 1: Sketch of (a) traditional small-loop TEM device with one transmitting coil and (b) small-loop TEM device with two opposing coils. Red arrows represent the direction **N** of global edges, green arrows represent the direction $\hat{\mathbf{n}}$ of transmitting current, and numbers are global node identifiers.
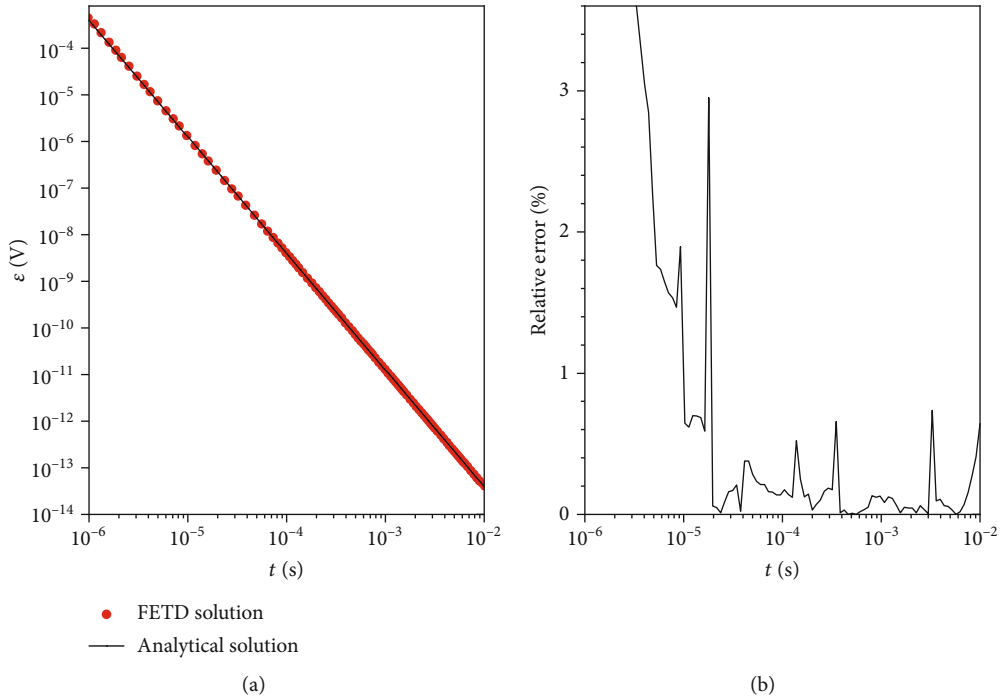

FIGURE 2: (a) The 3D FETD solution and the analytical solution and (b) the relative error between the two solutions of the half-space model.

3. Verification of Algorithm Accuracy

To test the reliability of the proposed algorithm, the TEM response of a half-space model is first calculated. In this model, a single-TX device of radius $R = 0.5$ m is placed at the origin with its axis in the z-direction, and the vertical induced electromotive force ε is calculated at the origin. The transmitting current I is 1A. The model is discretized

into 162719 tetrahedrons with 190779 edges in total, and it consists of an above air half-space and a below $\sigma = 10^{-2}$ S m^{-1}, $\mu = 4\pi \times 10^{-7}$ Hm^{-1} half-space. Then, the FETD solution is verified by the analytical solution [38].

$$\varepsilon = \frac{I}{\sigma R^3} \bullet \left[3 \operatorname{erf} (\theta R) - \frac{6\theta R + 4\theta^3 R^3}{\sqrt{\pi}} \bullet e^{-\theta^2 R^2} \right], \qquad (19)$$
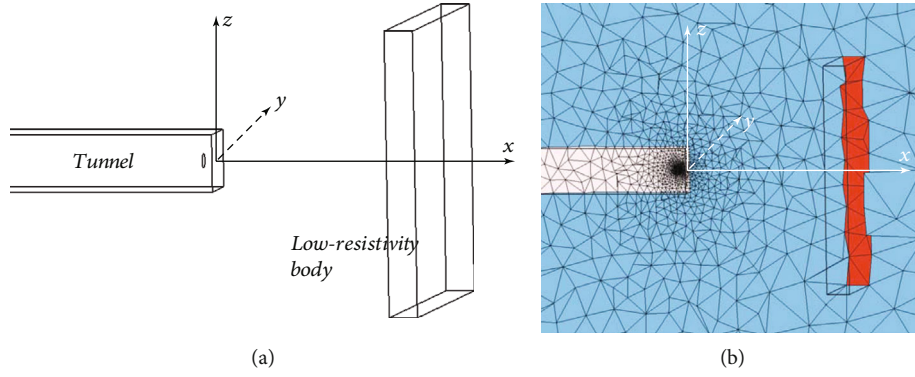
(a)

(b)

Figure 3: (a) Sketch of the synthetic tunnel TEM model and (b) cross-section of its tetrahedral meshing result.
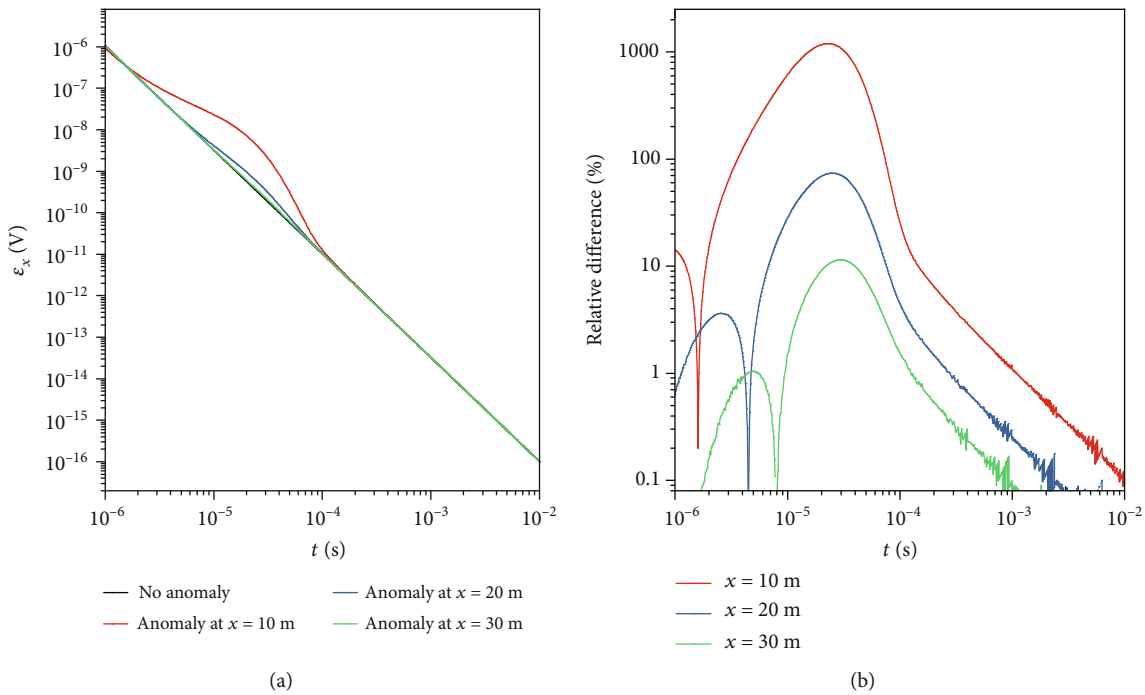

(a)

(b)

Figure 4: TEM response of the single-TX device. (a) ε_x response of the synthetic tunnel model without and with the low-resistivity anomaly at different positions. (b) Percentage relative difference of the ε_x response between models with and without the low-resistivity anomaly.

where erf represents the error function and parameter $\theta = \sqrt{\mu\sigma/4t}$.

We notice from Figure 2 that the FETD solution is well coincident with the analytical solution after 2×10^{-5} s. However, the numerical solution slightly deviates from the ideal case at early time channels. This is because both the primary transmitting field and the secondary inductive field contribute to the FETD solution, while only the secondary field contributes to the analytical solution. This is the FETD simulation of pulse width $t_p = 5 \times 10^{-7}$ s in this verification, which is more of an indication of the real world rather than an ideal situation. With regard to computational speed, the total simulation ends within 120 seconds, in which only 11 numerical factorizations and 254 backward substitutions are required.

4. Synthetic Tunnel Model Studies

In this section, the characteristics of tunnel TEM response are studied by synthetic model studies. In this model, a $\sigma = 1 \, \text{Sm}^{-1}$ brick abnormal body of 20 m wide and 5 m thick, is placed within the $\sigma = 10^{-2} \, \text{Sm}^{-1}$ background. As shown in Figure 3, the dimension of the tunnel is $2 \, \text{m} \times 2 \, \text{m}$, and it extends from the leftmost of the model to $x = 0$ m. Both the abnormal body and the tunnel are symmetric with respect to the x-axis.

4.1. Different Positions of Anomalies. One of the major concerns about the feasibility of the tunnel TEM prediction method is how well it could identify abnormal low-resistivity bodies [39–41]. Here, the single-TX transmitting
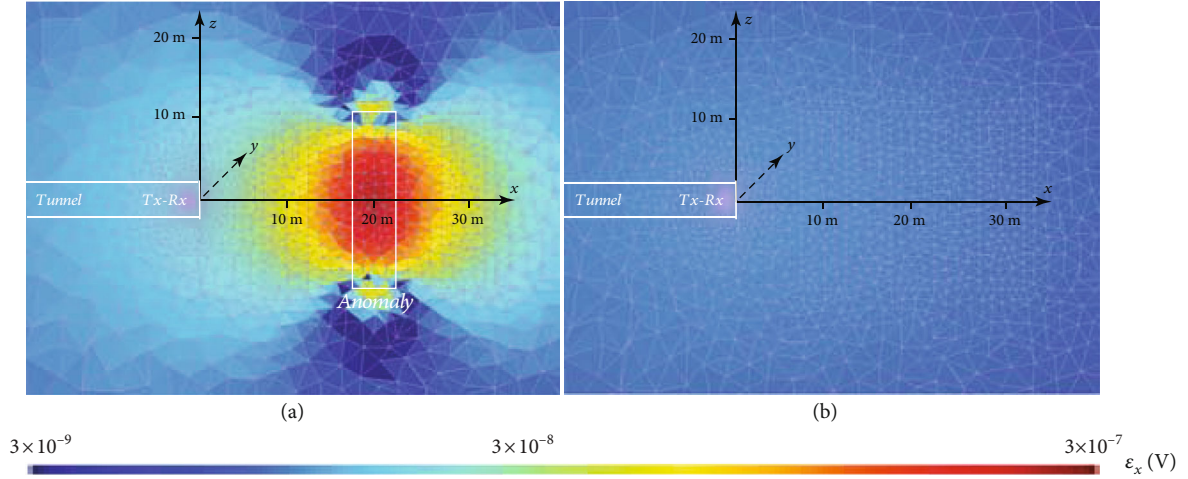
(a)   (b)

3×10^{-9} 3×10^{-8} 3×10^{-7}
ε_x (V)

FIGURE 5: Spatial ε_x response (a) with a low-resistivity body located at $x = 20$ m and (b) without any low-resistivity body in the xOz plane of the single-TX device at 2.5×10^{-5} s.

device is first studied. The coil has a radius of 0.5 m, and it is located at $x = -1$ m with its axis in the x-direction. The transmitting current of 1A keeps unchanged. Figure 4(a) gives the ε_x responses at the receiving point (-1 m, 0 m, and 0 m) with the low-resistivity body located at $x = 10$ m, 20 m, and 30 m, respectively. And percentage relative differences of ε_x between the three models with anomaly and the model without anomaly are given in Figure 4(b). It could be noticed that with the increase of buried depth, the relative difference between model responses with and without the low-resistivity body drops dramatically. Also, a small enough t_p must be chosen (in this example 10^{-6} s) to avoid the interference of the primary TEM field and to ensure the max relative difference occurs after the transmitting current turns off.

For a deeper understanding of the TEM response within a whole-space tunnel environment, the spatial distribution of the ε_x field at 2.5×10^{-5} s is given in Figure 5. We can observe that the transmitted electromagnetic field concentrates if a low-resistivity body exists. Contrarily, the ε_x field flattens out over the entire domain. This further suggests that the ε_x anomaly recorded by our TEM device is merely a repercussion of field enhancement in the distance. And if the ε_x data in some predrilling holes are collected, and more precise advanced detection results will be given.

4.2. The Presence of the Tunnel. Another concern about the feasibility of tunnel TEM detection is the presence of the empty tunnel. To evaluate this, model responses with and without the tunnel are compared in Figure 6, and the relative difference of ε_x is calculated similarly to that of Figure 4(b). In the model without a tunnel, its air conductivity 10^{-8} Sm^{-1} of the tunnel is replaced by the background conductivity 10^{-2} Sm^{-1}. And in both models, the same low-resistivity body is located at $x = 20$ m. Figure 6 shows that the existence of the tunnel has a negligible effect on the simulation result. This is because the tunnel can be regarded as an anomaly of high electric resistivity, which typically has minimal con-
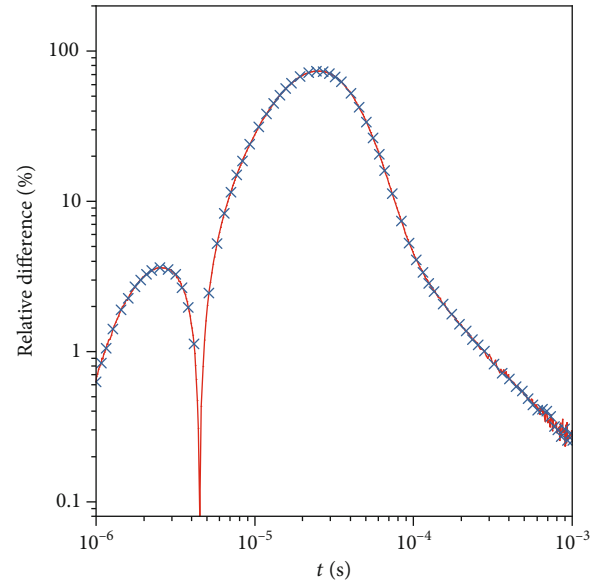

FIGURE 6: Percentage relative difference of ε_x with and without the low-resistivity anomaly at $x = 20$ m. The red line represents the relative difference of the model with a tunnel, while the blue cross line represents the relative difference of the model without a tunnel.

tribution to the total electromagnetic field. Therefore, we conclude that the presence of an empty tunnel does not impact the feasibility of tunnel TEM advanced detection.

4.3. Different Field Components. It is also noteworthy to understand the characteristics of the vertical ε_z response. Using the same single-TX model, the ε_z field is again calculated as shown in Figures 7 and 8. The most obvious feature is that the response curve goes through several sign reversals (Figure 7(a)) because of the nature of small-loop TEM devices. We also notice that the response patterns of the two models with the anomaly at $x = 20$ m and 30 m are quite similar to that of the model without the low-resistivity anomaly. This can be further explained in Figure 8, as the
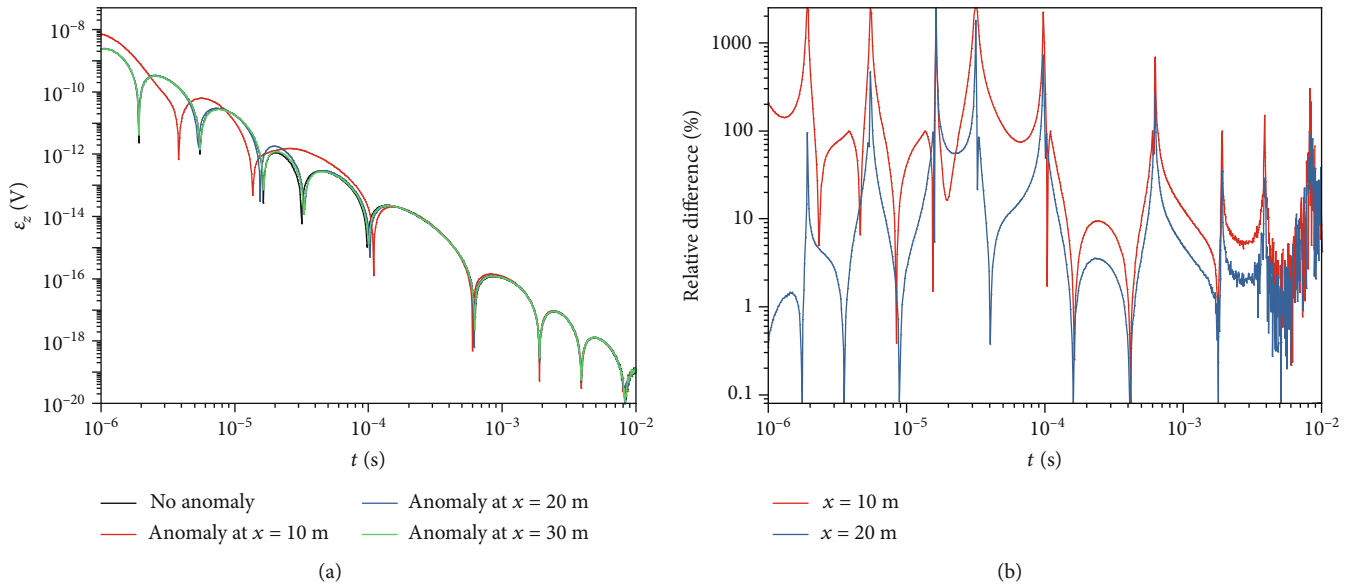
(a)

(b)

FIGURE 7: (a) ε_z response of the single-TX device. (b) Percentage relative difference of the ε_z response between models with and without the low-resistivity anomaly at $x = 10$ m, 20 m.
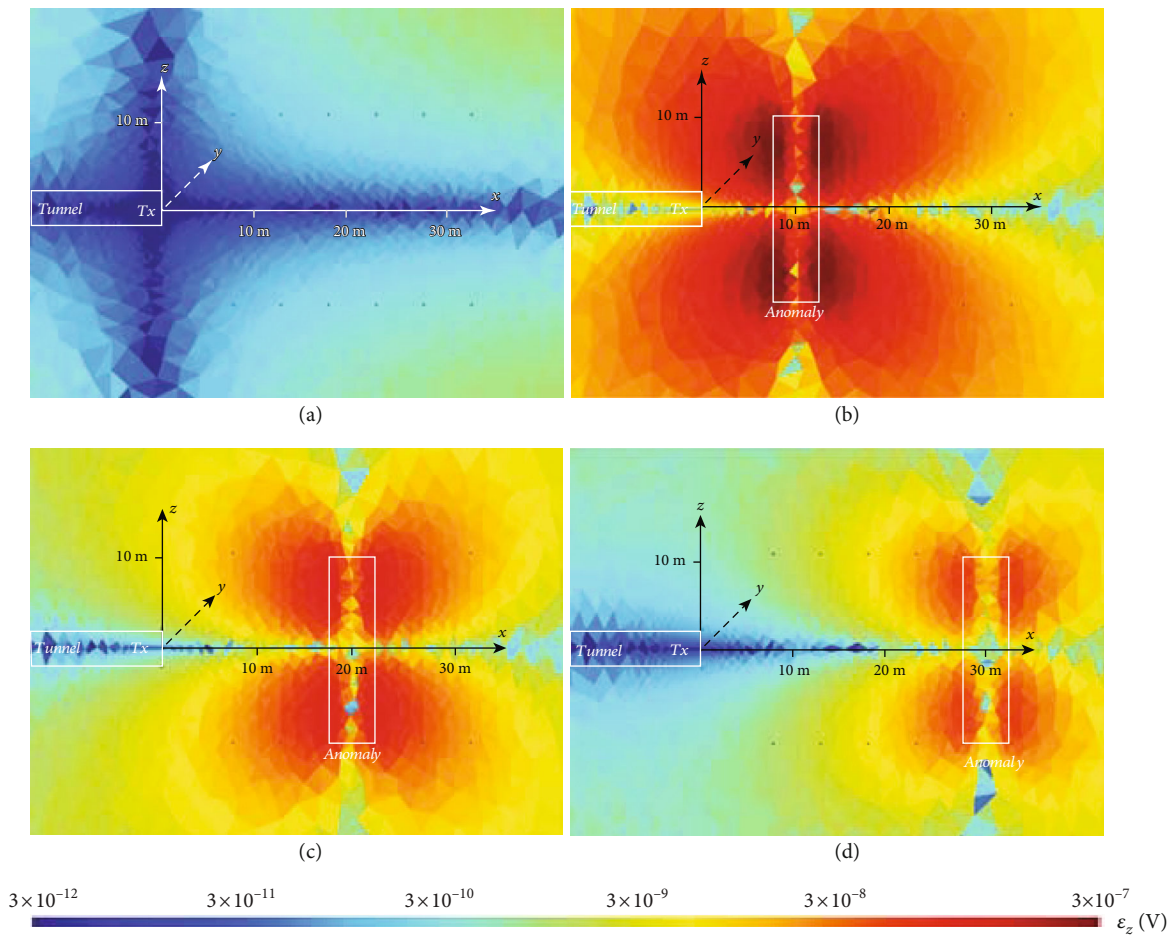

FIGURE 8: Spatial ε_z response (a) without any low-resistivity body and with a low-resistivity body located at (b) $x = 10$ m, c) $x = 20$ m, and d) $x = 30$ m in the xOz plane of the single-TX device at 2.5×10^{-5} s.
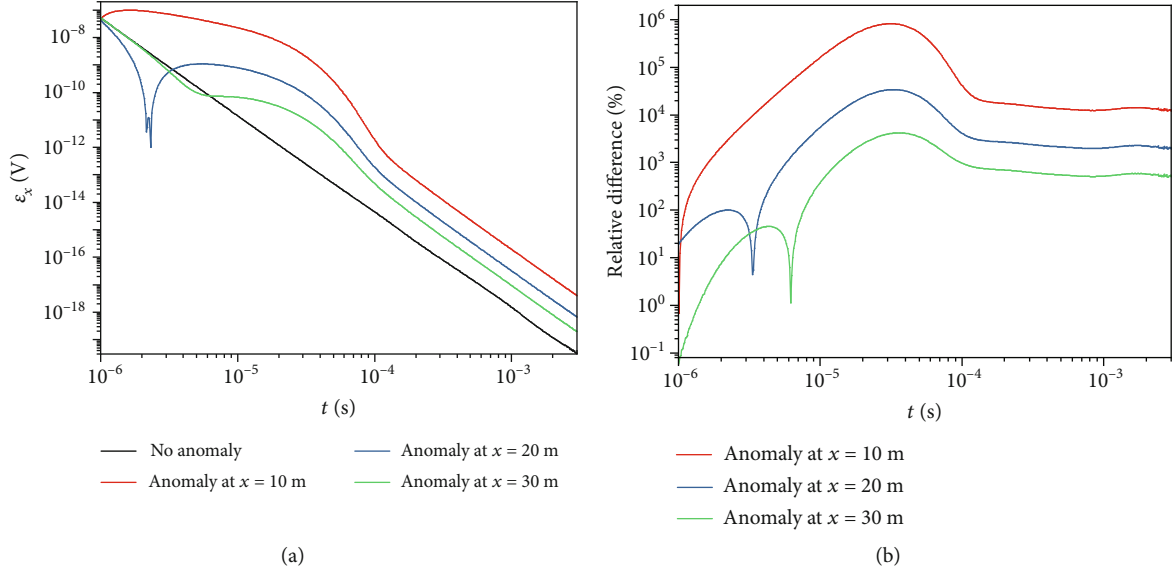
FIGURE 9: TEM response of the opposing-TX device. (a) ε_x response of the synthetic tunnel model without and with the low-resistivity anomaly at different positions. (b) Percentage relative difference of the ε_x response between models with and without the low-resistivity anomaly.
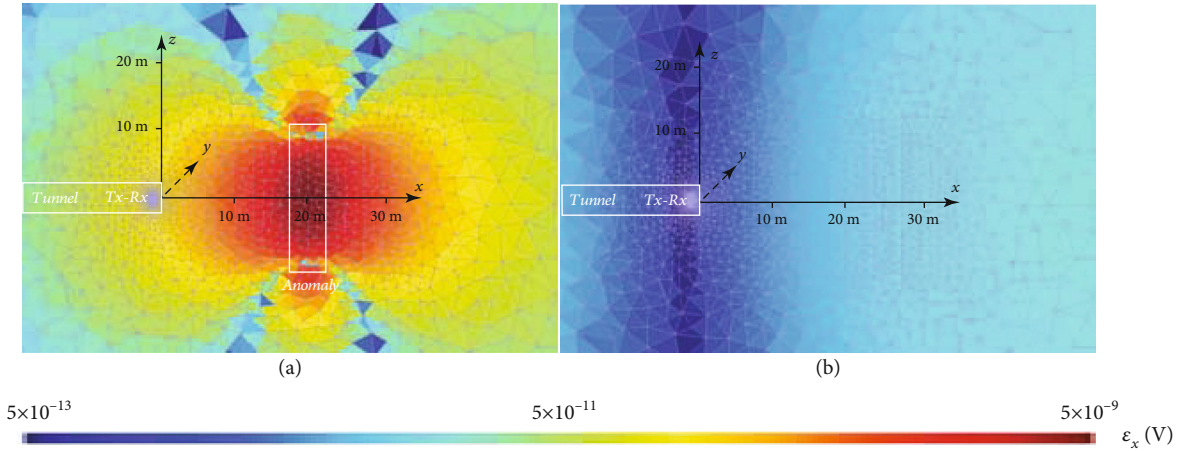

FIGURE 10: Spatial ε_x response (a) with a low-resistivity body located at $x = 20$ m and (b) without any low-resistivity body in the xOz plane of the opposing-TX device at 2.5×10^{-5} s.

ε_z field recorded by the single-TX device can be significantly affected by the anomaly at $x = 10$ m, while it is hard to be affected in the other two cases.

4.4. Different Types of Transmitting Coils. Here, the feasibility of the novel opposing-TX device is further studied. To achieve this, the same tunnel TEM model as the last simulation is utilized, with the only difference being that we replace the 0.5 m-radius coil with two coils carrying opposite directions of transmitting current. The two coils are spaced 0.2 m apart. And the center of the device, which is also the receiving point, keeps unchanged at $(-1$ m, 0 m, and 0 m). The ε_x response of the same abovementioned models is calculated as shown in Figures 9 and 10. We conclude from the comparison between Figures 4 and 9 that the opposing-TX device behaves with a much larger percentage difference

between models with and without the low-resistivity body over the entire observation period. However, its field amplitude is lower than that of the traditional single-TX device. From this forward modeling point of view, the opposing-TX device, which records pure secondary TEM field, is also suitable for tunnel advanced prediction.

5. Conclusions

This paper applies the FETD method to simulate the TEM response in a tunnel environment, offering a theoretical assessment of the effectiveness of the TEM method for advanced prediction in tunnels. Through tunnel model studies, we find that both the traditional single-TX device and the opposing-TX device are capable of revealing low-resistivity bodies. Nevertheless, the latter device performs

better in the relative difference of the axial ε_x field at the cost of a lower field amplitude. The presence of the high-resistivity tunnel has little influence on TEM advanced prediction. Meanwhile, it is also found that the horizontal field (the ε_x field in this paper) should be interpreted along with the vertical field (the ε_z field in this paper). Based on these 3D simulations, we conclude that the TEM method is crucial and feasible for tunnel advanced prediction, and that weak-coupling devices are promising for future fieldwork.

Data Availability

We confirm that no additional data is available.

Conflicts of Interest

The authors declare that they have no conflicts of interest regarding the publication of this paper.

Acknowledgments

References

[1] S. Shi, X. Xie, S. Tian et al., *Advanced Geological Prediction. In Tunnel Engineering-Selected Topics*, IntechOpen, London, UK, 2019.

[2] R. Otto, E. Button, H. Bretterebner, and P. Schwab, "The application of TRT-true reflection tomography-at the Unterwald tunnel," *Felsbau*, vol. 20, no. 2, pp. 51–56, 2002.

[3] J. Wang, J. Liu, F. Cheng, H. Yang, and Y. Huang, "Finite element reverse time migration imaging in tunnels using an unstructured mesh," *Applied Geophysics*, vol. 16, pp. 1–9, 2019.

[4] S. Li, B. Liu, L. Nie et al., "Detecting and monitoring of water inrush in tunnels and coal mines using direct current resistivity method: a review," *Journal of Rock Mechanics and Geotechnical Engineering*, vol. 7, no. 4, pp. 469–478, 2015.

[5] S. Qin, Z. Ma, C. Jiang et al., "Application of magnetic resonance sounding to tunnels for advanced detection of water-related disasters: a case study in the Dadushan tunnel, Guizhou, China," *Tunnelling and Underground Space Technology*, vol. 84, pp. 364–372, 2019.

[6] G. Lv, J. Ge, and L. Zhang, "Experimental research and application of tunnel transient electromagnetic leading detection remove noise method," *IOP Conference Series: Earth and Environmental Science*, vol. 358, no. 2, article 022008, 2019.

[7] N. V. da Silva, J. V. Morgan, L. MacGregor, and M. Warner, "A finite element multifrontal method for 3D CSEM modeling in the frequency domain," *Geophysics*, vol. 77, no. 2, pp. E101–E115, 2012.

[8] G. Zhou, M. Yue, X. Yang et al., "A metal interference correction method of tunnel transient electromagnetic advanced detection," *Journal of Geophysics and Engineering*, vol. 17, no. 3, pp. 429–438, 2020.

[9] G. V. Keller, "Electromagnetic surveys in the Central Volcanic Region," in *Geophysics Division Report, no. 55*, DSIR, Wellington, 1969.

[10] A. Hördt, V. L. Druskin, L. A. Knizhnerman, and K. M. Strack, "Interpretation of 3-D effects in long-offset transient electromagnetic (LOTEM) soundings in the Münsterland area/Germany," *Geophysics*, vol. 57, no. 9, pp. 1127–1137, 1992.

[11] G. Xue, L. Zhang, N. Zhou, and W. Chen, "Developments measurements of TEM sounding in China," *Geological Journal*, vol. 55, no. 3, pp. 1636–1643, 2020.

[12] Y. Liu and C. Yin, "3D inversion for multipulse airborne transient electromagnetic data," *Geophysics*, vol. 81, no. 6, pp. E401–E408, 2016.

[13] G. Xue, Y. Yan, X. Li, and Q. Di, "Transient electromagnetic S-inversion in tunnel prediction," *Geophysical Research Letters*, vol. 34, no. 18, 2007.

[14] X. Hu, P. Zhang, J. Yan, and L. Guo, "Improvement of means for interpretation of advanced water detection of tunnels by transient electromagnetic method," *Chinese Journal of Geotechnical Engineering*, vol. 36, no. 4, pp. 654–661, 2014.

[15] X. Shang, C. Jiang, Z. Ma, and S. Qin, "Combined system of magnetic resonance sounding and time-domain electromagnetic method for water-induced disaster detection in tunnels," *Sensors*, vol. 18, no. 10, p. 3508, 2018.

[16] L. Bu, S. Li, S. Shi et al., "Application of the comprehensive forecast system for water-bearing structures in a karst tunnel: a case study," *Bulletin of Engineering Geology and the Environment*, vol. 78, no. 1, pp. 357–373, 2019.

[17] J. Yu, R. Malekian, J. Chang, and B. Su, "Modeling of whole-space transient electromagnetic responses based on FDTD and its application in the mining industry," *IEEE Transactions on Industrial Informatics*, vol. 13, no. 6, pp. 2974–2982, 2017.

[18] C. Yin, Y. Qi, Y. Liu, and J. Cai, "3D time-domain airborne EM forward modeling with topography," *Journal of Applied Geophysics*, vol. 134, pp. 11–22, 2016.

[19] H. Fu, Y. Wang, E. S. Um et al., "A parallel finite-element time-domain method for transient electromagnetic simulation," *Geophysics*, vol. 80, no. 4, pp. E213–E224, 2015.

[20] Y. Ji, J. Lin, and Z. Wang, "Analysis and numerical removing of distortion in transient electromagnetic receiver device for shallow sounding," *Progress in Geophysics*, vol. 22, no. 1, pp. 262–267, 2007.

[21] Z. Fu, H. Wang, Y. Wang, N. Fu, H. M. Tai, and S. Qin, "Elimination of mutual inductance effect for small-loop transient electromagnetic devices," *Geophysics*, vol. 84, no. 3, pp. E143–E154, 2019.

[22] Z. Xi, X. Long, L. Huang et al., "Opposing-coils transient electromagnetic method focused near-surface resolution," *Geophysics*, vol. 81, no. 5, pp. E279–E285, 2016.

[23] P. Xiao, Z. Shi, X. Wu, and G. Fang, "Improved bucking coil design in helicopter transient electromagnetic system," *Progress In Electromagnetics Research M*, vol. 60, pp. 131–139, 2017.

[24] Y. Goldman, C. Hubans, S. Nicoletis, and S. Spitz, "A finite-element solution for the transient electromagnetic response of an arbitrary two-dimensional resistivity distribution," *Geophysics*, vol. 51, no. 7, pp. 1450–1461, 1986.

[25] J. M. Jin, *The Finite Element Method in Electromagnetics*, John Wiley & Sons, 2015.

[26] J. C. Nédélec, "Mixed finite elements in $\mathbb{R}^3$," *Numerische Mathematik*, vol. 35, no. 3, pp. 315–341, 1980.

[27] G. Lindfield and J. Penny, *Numerical Methods: Using MATLAB*, Academic Press, 2018.

[28] E. S. Um, J. M. Harris, and D. L. Alumbaugh, "3D time-domain simulation of electromagnetic diffusion phenomena: a finite-element electric-field approach," *Geophysics*, vol. 75, no. 4, pp. F115–F126, 2010.

[29] B. P. Flannery, W. H. Press, S. A. Teukolsky, and W. Vetterling, *Numerical recipes in C*, Press Syndicate of the University of Cambridge, 1992.

[30] D. Ge and B. Wei, *Time Domain Computational Method for Electromagnetic Waves*, Xidian University Publishing House, 2015.

[31] X. Yang, M. Yue, D. Hu, Y. Li, and X. Wu, "Goal-oriented 3-D time-domain marine CSEM modeling with anisotropy and topography," *IEEE Transactions on Geoscience and Remote Sensing*, vol. 60, pp. 1–14, 2022.

[32] B. Delaunay, "Sur la sphere vide," *Izv. Akad. Nauk SSSR, Otdelenie Matematicheskii i Estestvennyka Nauk*, vol. 7, no. 793-800, pp. 1-2, 1934.

[33] C. Geuzaine and J. F. Remacle, "Gmsh: a 3-D finite element mesh generator with built-in pre- and post-processing facilities," *International Journal for Numerical Methods in Engineering*, vol. 79, no. 11, pp. 1309–1331, 2009.

[34] Y. Saad, *Iterative Methods for Sparse Linear Systems*, Society for Industrial and Applied Mathematics, 2003.

[35] X. Li and J. W. Demmel, "SuperLU_DIST: a scalable distributed-memory sparse direct solver for unsymmetric linear systems," *ACM Transactions on Mathematical Software*, vol. 29, no. 2, pp. 110–140, 2003.

[36] O. Schenk, K. Gärtner, W. Fichtner, and A. Stricker, "PARDISO: a high-performance serial and parallel sparse linear solver in semiconductor device simulation," *Future Generation Computer Systems*, vol. 18, no. 1, pp. 69–78, 2001.

[37] I. S. Duff, M. A. Heroux, and R. Pozo, "An overview of the sparse basic linear algebra subprograms: the new standard from the BLAS technical forum," *ACM Transactions on Mathematical Software*, vol. 28, no. 2, pp. 239–267, 2002.

[38] X. Yang, X. Wu, and M. Yue, "A fast 3-D finite element modeling algorithm for land transient electromagnetic method with OneAPI acceleration," *Computers & Geosciences*, vol. 166, article 105186, 2022.

[39] X. Lu, X. Hu, Z. Xu et al., "Tunnel concealed karst cave joint detection by tunnel seismic and transient electromagnetic," *Lithosphere*, vol. 2022, no. 1, Article ID 2827582, 2022.

[40] Q. Li, Y. Han, X. Liu, U. Ansari, Y. Cheng, and C. Yan, "Hydrate as a by-product in CO2 leakage during the long-term sub-seabed sequestration and its role in preventing further leakage," *Environmental Science and Pollution Research*, vol. 29, no. 51, pp. 77737–77754, 2022.

[41] Q. Li, F. Wang, Y. Wang et al., "Effect of reservoir characteristics and chemicals on filtration property of water-based drilling fluid in unconventional reservoir and mechanism disclosure," *Environmental Science and Pollution Research*, vol. 30, no. 19, pp. 55034–55043, 2023.